Precipitation and strengthening modeling for disk-shaped particles in aluminum alloys: size distribution considered

Yue Li , Bjørn Holmedal , Hongxiang Li , Linzhong Zhuang , Jishang Zhang , Qiang Du

PII: S2589-1529(18)30189-3
DOI: https://doi.org/10.1016/j.mtla.2018.11.001
Reference: MTLA 152

To appear in: *Materialia*

Please cite this article as: Yue Li , Bjørn Holmedal , Hongxiang Li , Linzhong Zhuang , Jishang Zhang , Qiang Du , Precipitation and strengthening modeling for disk-shaped particles in aluminum alloys: size distribution considered, *Materialia* (2018), doi: https://doi.org/10.1016/j.mtla.2018.11.001

Precipitation and strengthening modeling for disk-shaped particles in aluminum alloys: size distribution considered

Yue Li[1,2,3], Bjørn Holmedal[3], Hongxiang Li[1,*], Linzhong Zhuang[1,4], Jishang Zhang[1], Qiang Du[2,*]

[1]State Key Laboratory for Advanced Metals and Materials, University of Science and Technology Beijing, 100083, Beijing, China

[2]SINTEF Industry, 0314, Oslo, Norway

[3]Norwegian University of Science and Technology, 7491, Trondheim, Norway

[4]Tata Steel, 1970 CA Ijmuiden, Netherlands

*Corresponding author, Qiang Du, Tel.:+47 93401069, E-mail address: qiang.du@sintef.no

Hongxiang Li, Tel.: +86-10-62332350, E-mail address: hongxiang_li@vip.163.com;

Abstract

For an ICME (Integrated Computational Material Engineering) modeling framework used for the age-hardening aluminum alloy design and heat treatment parameters optimization, it is critical to take into account the geometric shape of precipitates, as it is tightly related to the precipitation kinetics and particles' hardening effect. The aim of this paper is to present such an ICME modeling approach to describe the precipitation of disk-shaped hardening particles during aging treatment and predict the final yield strength. The classical Kampmann-Wagner Numerical (KWN) model is extended to consider the influence of disk-shaped particle morphology on growth kinetics. The extension consists of two correction factors to the growth rate equation and to the Gibbs-Thomson effect. The extended model, coupled with a metastable thermodynamic database, is applied to simulate precipitation kinetics of Al-Cu and Al-Mg-Zn alloys during aging treatment. The predicted microstructural features are in reasonable agreement with the reported experimental observations. Furthermore, a strengthening model for disk-shaped particles, which considers the size distributions of precipitates, is developed. The predicted yield strengths are compared with reported tensile test results and with predictions from other strength models. Unlike other models, the proposed strength model can reveal the strength contribution from disk-shaped precipitates without an additional tuning parameter for accounting for the impact of the mean particle spacing in the slip plane.

Keywords: Age-hardening alloys; Disk-shaped particles; Precipitation kinetics; Mechanical properties; Modeling

1. Introduction

The shape of hardening particles in heat-treatable aluminum alloys is often non-spherical. Typical examples are needle-shaped β″ precipitates in Al-Mg-Si [1] and disk-shaped θ′ precipitates in Al-Cu [2] alloys. Previously, many microstructure and mechanical properties models employed an assumption of spherical precipitates [3-5]. However, the development of models for microstructure evolution and strength for non-spherical particles (including needle, disk, and other complex shapes) is crucial for the Integrated Computational Materials Engineering (ICME) framework to optimize industrial alloy compositions and heat treatment processes for metallic materials [6].

Research efforts towards microstructure modeling have been reported such as the ones listed in [6-10], and they can be divided into two categories: The Frequency Distribution Function (FDF) approaches and the Direct Detailed Numerical approaches (DDN) [11]. The former is represented by Kampmann-Wagner Numerical (KWN) approach and the later by the phase field method. The FDF approaches have been successfully applied to predict the as-cast grain size of inoculated multi-component aluminum alloys [12], model the homogenization process in Al-Mn-Fe-Si alloys [13] and Al-Mg-Si-Fe-Mn alloys [14, 15], as well as to simulate concurrent nucleation, growth, and coarsening of multi precipitates during aging treatment in Al-Mg-Si alloys [16]. One of the important features of the FDT approaches is that the model is able to treat the statistical distribution of a specific microstructure feature. When it comes to the applications within industrial alloy design/processing parameter optimization problems, this type of approaches are superior to the accurate, but computationally-expensive, phase field approach [16] in which the detailed spatial distributions of microstructure features are predicted. The KWN method excels at addressing the multi-scale and multi-component industrial problems due to its mathematical simplicity and convenient coupling with the CALPHAD database. Both of the two approaches have been applied to non-spherical particles growth [6, 8, 10]. The computationally expensive phase field method can even be employed to pin down the most important physical properties in determining the final shape of precipitates for Al-Cu alloys, i.e. the growth anisotropy [10].

Disk-shaped or plate-shaped hardening particles are encountered during aging treatment of many different alloy systems. Examples include disk θ′ particles in Al-Cu [2], lath S particles in Al-Cu-Mg [17], platelet η' particles in Al-Zn-Mg [18], plate β_2' particles in

Mg-Zn [19], plate γ' particles in Mg-Y-Zn [20], disk γ'' particles in Inconel 718 [21], and disk $\delta - Ni_2Si$ particles in Cu-Ni-Si alloys [22]. The KWN approach needs to be extended to enable its application to these industrial alloys. Such an extension is straightforward following the methodology, earlier applied successfully to needle-shaped particles in Refs. [6, 8].

The extension involves a full analytical solution to the volume diffusion-controlled growth of the particles and approximate treatment of Gibbs–Thomson effect. The diffusion solution for oblate spheroids with constant aspect ratio was provided by Ham [23] and by Horvay and Cahn [24] (HHC). Chen and Doherty [25] applied the HHC theory to Al-Cu alloys and compared the predicted growth rates with the measured values. Liu et al. [26] also utilized the HHC theory but adapted the original equations to model the aging process of heat-treatable aluminum alloys containing plate/disc- or rod/needle- shaped precipitates. Recently, this method has been adopted by Hu et al. [27] to predict the growth process of disk-shaped θ' precipitates in Al-Cu-Cd alloys. The mathematical problem related to non-spherical particle growth is also of interests to the researchers in other disciplines. In a work considering the inorganic carbon uptake by phytoplankton, Wolf-Gladrow and Riebesell [28] found that the increase in the surface to volume ratio of spheroids enhances the potential supply of solutes per unit cell. Thus, they proposed a surface area equivalent concept to treat non-spherical particle's growth.

Recently two simple correction factors were introduced to describe the effects of the particle shape on growth kinetics [6, 8]. The general idea was to obtain one correction factor by solving the steady-state diffusion problem for the particle shape of interest. The other factor modifies the Gibbs–Thomson effect and can be derived from the Gibbs energy minimization principle for the considered particle shape. Holmedal et al. [6, 8] worked out correction factors for needle-shaped particles, based on the analytical solution of the diffusion problem by Ham [23, 29], and by numerical solution of the diffusion problem for cuboid shapes. The correction factors were implemented into a KWN model framework and tested by predicting the precipitation kinetics of needle-shaped β'' precipitates in Al-Mg-Si alloys [6, 8], where these extensions led to a better agreement with the experimental measurements on particle size distributions.

The concept of applying two correction factors was later adopted in the Thermo-calc software [30, 31], following the methodology suggested in [6, 8]. They considered spheroid shapes and applied the same analytical solution of the diffusion solution by Ham [23, 29], but also included oblate spheroid shapes as an approximation of disk-shaped precipitates. They took a step further to account for shape evolution by minimizing the sum of coherent elastic

strain energy and interfacial energy. However, their correction factor for the Gibbs Thomson effect differs significantly from the one suggested by Holmedal et al. [6, 8]. Their treatment of the Gibbs Thomson effect follows the classical treatment in Ref. [32]. It is simply assumed that the particle surface will have the equilibrium shape, allowing both curvature and facets with corners, and that this shape is dictated by the anisotropy of the surface energy according to the Wulff's solution. The surface energy must be specified only at one reference point at the particle surface, its further directional variation is dictated by the prescribed particle shape. For this treatment, it corresponds to, that the particle grows fastest in directions normal to particle surface parts with lowest surface energy. This is not the case when the particle has coherent or partly coherent surfaces that are constrained from bowing out, i.e. surface growth in the surface normal direction is constrained and surface curvature is restricted. For example, the β'' precipitates considered in [6, 8] are needle shaped with a higher surface energy for their end surfaces than for their coherent side surfaces, but they still increase their aspect ratio by elongating faster in their needle direction. The reason is that the surface formation is constrained. When a particle is forced to remain cuboid in shape and only grows in the needle direction, the areas of the top and bottom surfaces of the needle remain the same, and only new side surfaces are created. This has a low cost in terms of surface energy. When the needle thickens, the energy cost is mainly due to the increased areas of the needle end surfaces corresponding high surface energy. The treatment of Gibbs Thomson effect from Thermo-calc software [30, 31] has the potential to be extended to account for the growth constraints.

In this paper, the same methodology as the one employed for prolate-shaped particles [6, 8] is applied to describe the growth kinetics of disk-shaped particles. The different treatments mentioned above will be evaluated in Section 2.1. Such an evaluation, which is lacking in the literature, is useful for any further development along this research front. Finally, a reasonable treatment is chosen and combined with the correction factor for the Gibbs-Thomson effect to extend the KWN model.

Another novelty of this work is to propose a strength model for disk-shaped particles. Thus, the importance of introducing particle morphology and particle size distributions in the whole ICME framework is further revealed. Earlier works [3, 4, 9, 26, 27, 33-36] deal with strength contributions from precipitates according to the theories by Friedel [37] and Kocks [38]. In these theories two parameters are required, i.e. the mean distance between dislocation obstacles in the slip plane and the mean obstacle strength. In terms of estimating the mean distance between dislocation obstacles in the slip plane, it is quite common to use a simplified model based on the mean particle spacing in the slip plane, assuming that the particles are

uniformly distributed and have the mean size [3, 4, 9, 26, 27, 33-36]. Note that previous strength models for non-spherical precipitates [3, 4, 9, 27, 34, 35] provide different models for strong and weak particles [9, 34, 35] or introduce an additional calibration parameter to treat the strength contribution from non-spherical precipitates [3, 4, 27]. For the second parameter, the mean obstacle strength, a common way is to make an average of the strengths of all precipitates [3, 4]. However, it is well known that thin, long, needle-shaped precipitates pierce many slip planes and therefore contribute with a higher number of dislocation obstacles than spherical particles [39]. It can be further improved by using an average of the strengths of all particle-based dislocation obstacles in the slip plane considering the size and shape distributions of the precipitates. This strength model has been applied to the AA6082 alloy [39]. This current paper provides an extension of this strength model to cases of disk-shaped precipitates. Furthermore, an integration of the extended KWN and the strength model is made, using the predicted size distribution of the precipitates as input. The integrated framework is verified by simulating precipitation kinetics and strengthening responses of binary Al-Cu and ternary Al-Mg-Zn alloys during aging.

The goal of the paper is to reveal the effects of particle shape and size distribution on precipitation kinetics and mechanical properties. The paper is organized as follows. Section 2 describes the extended KWN model for disk-shaped precipitates. Section 3 concentrates on the novel strength model for disk-shaped precipitates. Section 4 compares the reported experimental data with the predicted results. A discussion is given in Section 5.

2. The extension of the KWN model toward disk-shaped particles

Previously, the KWN model for needle-shaped precipitates has been reported in [6, 8]. The KWN modeling framework of the current model is quite similar and not described here. The new extension consists of two correction factors: one is for growth rate equation and the other is for Gibbs-Thomson effect. They are described in the following two subsections.

2.1. The correction factor for growth rate equation

For diffusion-controlled growth, the key in deriving the growth rate is to calculate the diffusional transportation rate of solute to the migrating interface. Following Ham's treatment [23], a disk-shaped precipitate is approximated as an oblate spheroid, as shown in Figure 1, with a thickness of L and radius of r_0:

$$\frac{x^2 + y^2}{r_0^2} + \frac{4z^2}{L^2} = 1 \tag{1}$$

Here $L/2 < r_0$. The aspect ratio is defined as $\alpha = L/(2r_0)$. The volume, V, of the oblate spheroid is

$$V = \frac{2\pi}{3} r_0^2 L \tag{2}$$

The eccentricity *e* and surface area, *S* are given by

$$e = \sqrt{1 - \frac{L^2}{4r_0^2}} = \sqrt{1 - \alpha^2} \tag{3a}$$

$$S = 2\pi r_0^2 \left(1 + \frac{1 - e^2}{e} \tanh^{-1} e\right) \tag{3b}$$

It is useful to define a radius, *R*, of an equivalent sphere (see Figure 1), whose volume is identical to the spheroid:

$$R = \sqrt[3]{\frac{L r_0^2}{2}} \tag{4}$$

As to be shown later, the precipitation kinetics of the spheroid particle and its spherical equivalent are closely related.

The oblate spheroidal coordinate is employed in the following analysis. The relationship between oblate spheroidal coordinates and Cartesian coordinates is as follows:

$$x = a\xi\eta\cos\phi \tag{5a}$$

$$y = a\xi\eta\sin\phi \tag{5b}$$

$$z^2 = a^2(\xi^2 - 1)(1 - \eta^2) \tag{5c}$$

Here,

$$a = \frac{1}{2}\sqrt{4r_0^2 - L^2} \tag{5d}$$

Here $\xi \in [1, \infty), \eta \in [-1, 1]$, and $\phi \in [0, 2\pi)$.

It is assumed that the compositional profile of solute *i* in the front of the migrating precipitate-matrix interface satisfies the steady-state diffusion equation, and that the boundary conditions at the migrating interface and at the far-field boundary are angle-independent. Therefore we have

$$\nabla^2 c_i = 0 \tag{6}$$

with the boundary conditions of $c_i = c_i^m$ for $\xi \to \infty$, i.e. on a sphere of infinite radius, and $c_i = c_i^m + \Delta c_i$ on the oblate surface, i.e. $\xi = \xi_0 = 2r_0/\sqrt{4r_0^2 - L^2}$.

According to the analytical solutions of Eq. (6) found in reference [23] for oblate spheroids, the compositional profile surrounding a growing spheroid with the dimension of ξ_0 is described by:

$$c_i(\xi) = c_i^m + \Delta c_i \left(1 - \frac{\arccos(\xi^{-1}) - \arccos(\xi_0^{-1})}{\arcsin(\xi_0^{-1})}\right) \tag{7}$$

Eq. (7) should be contrasted with the compositional profile surrounding the equivalent volume spherical precipitate:

$$c_i^{\text{spherical}}(r) = c_i^m + \frac{\Delta c_i}{r}\sqrt[3]{\frac{Lr_0^2}{2}} \tag{8}$$

Here $r = \sqrt{x^2 + y^2 + z^2}$. From the compositional profiles expressed by Eq. 7 and Eq. 8, the following equation can be derived to calculate the flux J_i^{oblate} of solute *i* through the precipitate interface for the oblate spheroid, and the flux for the equivalent volume sphere, $J_i^{\text{spherical}}$, respectively:

$$J_i^{\text{oblate}} = \iint_s (\boldsymbol{I}.\boldsymbol{n}) dA \tag{9}$$

Here $\boldsymbol{n}$ is the unit vector normal to the precipitate interface. A vector $\boldsymbol{I}$, with opposite direction from $\boldsymbol{n}$, gives the flux of solute *i* per unit area.

$$\boldsymbol{I} = -D_i \frac{1}{a}\sqrt{\frac{\xi^2 - 1}{\xi^2 - \eta^2}}\frac{\partial c_i}{\partial \xi} \tag{10a}$$

$$dA = a^2\sqrt{\frac{\xi^2 - \eta^2}{1 - \eta^2}}\xi\eta d\eta d\phi \tag{10b}$$

Thus,

$$J_i^{\text{oblate}} = \frac{4\pi D_i \Delta c_i r_0 e}{\arcsin e} = \frac{4\pi D_i \Delta c_i r_0 e}{\arctan\left(\frac{e}{\sqrt{1 - e^2}}\right)} \tag{11a}$$

$$J_i^{\text{spherical}} = 4\pi D_i \Delta c_i \sqrt[3]{\frac{1}{2} Lr_0^2} \tag{11b}$$

The following solute conservation law should be satisfied at the migrating interface:

$$J_i dt = \left(c_i^m + \Delta c_i - c_i^p\right)\, dV \tag{12}$$

where c_i^p is the solute concentration (per volume) of solute *i* in the particle.

The rates of the volume change of the oblate spheroid ($\dot{V}^{\text{oblate}}$) and the equivalent volume sphere ($\dot{V}^{\text{spherical}}$) are derived from Eqs.11a and 11b, respectively:

$$\dot{V}^{\text{oblate}} = \frac{4\pi D_i \Delta c_i r_0 e}{\left(c_i^m + \Delta c_i - c_i^p\right)\arctan\left(\frac{e}{\sqrt{1 - e^2}}\right)} \tag{13a}$$

$$\dot{V}^{\text{spherical}} = \frac{4\pi D_i \Delta c_i}{\left(c_i^m + \Delta c_i - c_i^p\right)}\sqrt[3]{\frac{r_0^2 L}{2}} \tag{13b}$$

Thus,

$$f(\alpha) = \frac{\dot{V}^{\text{oblate}}}{\dot{V}^{\text{spherical}}} = \frac{\sqrt{1-\alpha^2}}{\sqrt[3]{\alpha}\arccos\alpha} \tag{14}$$

where $f(\alpha)$ is the correction factor for growth rate equation. In the asymptotic limit of small aspect ratios, it can be found as $f(\alpha) = 2/(\pi\sqrt[3]{\alpha})$. Thus, the growth rate of the radius of the spherical particle with equivalent volume and the same amount of diffusion flux can be expressed as:

$$\frac{\mathrm{d}R}{\mathrm{d}t} = \frac{f(\alpha)\Delta c_i D_i}{\left(c_i^m + \Delta c_i - c_i^p\right)R} \tag{15}$$

t is the time.

For multi-component systems ($i > 1$), the Eq. 15 is written as:

$$\frac{\mathrm{d}R}{\mathrm{d}t} = \frac{f(\alpha)\Delta c_1 D_1}{\left(c_1^m + \Delta c_1 - c_1^p\right)R} \tag{15.1}$$

$$\frac{D_i\Delta c_i}{(c_i^m+\Delta c_i-c_i^p)} = \frac{D_1\Delta c_1}{(c_1^m+\Delta c_1-c_1^p)} \text{ for } i \geq 2. \tag{15.2}$$

The dependence of the proposed correction factor for growth rate equation on the aspect ratios is shown in Figure 2. With the aspect ratio decreasing from 1 to 0.01, the correction factor increases from 1 to 3. Compared with the spherical shape, the oblate shape enhances the solute atom transportation rate to the migrating interface, and thus increases the growth rate of the precipitate. The introduction of the growth rate correction factor can be regarded as a modification of the diffusivity D_i, if the precipitate shape remains unchanged.

In addition, the correction factors reported in Ref. [25, 26, 28] are also derived (see **Appendix A**) and compared with the proposed correction factor in Figure 2. Note that Chen and Doherty's correction factor is supersaturation-dependent, and a Matlab script was made to solve the nonlinear equation A3 iteratively, and then to derive the correction factor for each supersaturation. As can be seen from Figure 2, the correction factor from Chen and Doherty [25] increases more sharply with decreasing aspect ratio when the supersaturation increases. When the supersaturation is very low, results from Chen and Doherty's [25], Wolf-Gladrow and Riebesell's [28], and our proposed method are quite close. In comparison, Liu et al.'s result [26] is smaller than the others. Moreover, when the aspect ratio is equal to one, the correction factor from Ref. [26] is significantly smaller than unity, and the one from Ref. [25] decreases from about 1.6 at the supersaturation of 0.1 to close to 1.0 at the supersaturation of 0.0005. Only Wolf-Gladrow and Riebesell's [28] and our models degenerate to the spherical case.

Among these four correction factors, it is found that Liu et al.'s [26] method underestimates the growth rate of oblate-shaped particles and also does not degenerate to the

spherical one when the aspect ratio is equal to one. Wolf-Gladrow and Riebesell's [28] method is based on the hypothesis that the correction factor can be estimated from the surface area of the non-spherical particle, so their results need to be verified by much more detailed mathematical solutions such as the phase field method. The correction factor from Chen and Doherty [25] depends on both the supersaturation and aspect ratio and may be a better choice in handling solute-rich alloys such as Ni-based superalloys. However, it is not straightforward to employ this correction factor to extend the KWN model. For the age-hardening aluminum alloy with low supersaturation, the model proposed can predict its microstructural evolution with good numerical efficiency and robustness.

The particles sometimes are better approximated by a cuboid plate shape as shown in Figure 4. For this geometry, a numerical solution of the diffusion solution was carried out. The numerical solution is the same as reported in [8] for cases of cuboid needle-shaped particles, except for the choice of aspect ratio smaller than one. Hence, details about the simulations are not described here. For small aspect ratios, the diffusion is controlled by the plate area of the particle, and an asymptotic solution can be found (numerical) as $f(\alpha) = 0.59/\sqrt[3]{\alpha}$. This solution is similar as for the oblate spheroid shape with the same $\alpha^{-1/3}$ dependency, and for aspect ratios $\alpha < 0.1$ this is a good approximation. The correction factor for cuboid plates from the numerical simulations is included in Figure 2 and is very close to the proposed method. Note that the volume of a cuboid plate particle is larger than of an oblate-shaped particle with the same aspect ratio.

2.2. The correction factor for the Gibbs-Thomson effect

Due to the Gibbs-Thomson effect, Δc_i is modified differently along the precipitate interface due to the interfacial energy anisotropy leading to a variation of local mean curvature, γ, which is given by:

$$\gamma = \frac{L\left(2r_0^2 + \left(\frac{L^2}{4} - r_0^2\right)cos^2\beta\right)}{4r_0\left(r_0^2 + \left(\frac{L^2}{4} - r_0^2\right)cos^2\beta\right)^{3/2}}, \qquad -\frac{\pi}{2} < \beta < \frac{\pi}{2} \tag{16}$$

Here β is the parametric latitude. As mentioned in the previous work [8], the treatment of the variation of solute concentration along a non-spherical particle interface is a difficult task. In [8], two simplified approximate methods were considered, both assuming that the shape of the particle is known a priori and changing slowly. Note that this type of model accounts for the effects induced by shape change on growth rate but cannot be applied to predict the shape change. One way to simplify the mathematical treatment is to apply averages of the interfacial energy and of the local curvature variation, i.e. to assume that the Gibbs-Thomson

effect to the interfacial matrix composition on the whole non-spherical surface is represented by the average local mean curvature of the spheroid surface, γ_{mean}.

$$\gamma_{\text{mean}} = \frac{1}{\pi}\int_{-\frac{\pi}{2}}^{\frac{\pi}{2}} \frac{\frac{L}{2}\left(2r_0^2 + \left(\frac{L^2}{4} - r_0^2\right)cos^2\beta\right)}{2r_0\left(r_0^2 + \left(\frac{L^2}{4} - r_0^2\right)cos^2\beta\right)^{\frac{3}{2}}} d\beta \tag{17}$$

Thus, the correction factor due to Gibbs-Thomson effect is given:

$$g(\alpha)_{\text{mean}} = R\gamma_{\text{mean}} \tag{18a}$$

For the case of a cuboid shape with sharp corners, the local curvature cannot be applied. Instead, another approach was applied in [8], taking into account the increase in free energy due to the presence of the particle interface. This methodology for the Gibbs-Thomson effect of prolate-shaped and cuboid needle-shaped particles was reported in [8]. For the oblate spheroid this methodology gives a correction factor:

$$g(\alpha)_{\text{oblate}} = \frac{1}{2\alpha^{\frac{2}{3}}}\left(1 + \frac{\alpha^2}{\sqrt{\alpha^2 - 1}}\tanh^{-1}\sqrt{1 - \alpha^2}\right) \tag{18b}$$

For the case of the cuboid plate particle with aspect ratio β (the ratio of thickness and width), the correction factor is the same as given in [8] for the case of needle shaped particles:

$$g(\beta)_{\text{cuboid}} = \frac{(2\beta + 1)}{2\pi}\left(\frac{4\pi}{3\beta}\right)^{\frac{2}{3}} \tag{18c}$$

The interfacial phase composition, both for cases of oblate-shaped or cuboid particles, can be calculated by applying one of the suggested correction factors:

$$c_i = c_i^m + \Delta c_i = c_i^m \exp\left(\frac{2g\sigma V_m^\gamma}{X_i^\gamma RKT}\right) \tag{19}$$

Here σ is the interfacial energy. V_m^γ is the average molar volume of γ phase. K and T are the Boltzmann constant and temperature, respectively. X_i^γ is the molar fraction of element i in the γ phase.

Figure 3 plots the dependencies of the second correction factor, g, on the aspect ratio for the three cases considered above. In all three cases, the correction factor increases with decreased aspect ratio, except for a slight decrease close to unity for the mean curvature approximation. This means that the Gibbs-Thomson effect will increase the interfacial solute content, which decreases the solute supplement to precipitates and thus lower precipitate growth rate. This is opposite to the effect of the first correction factor. The second correction factor could be regarded as a modification of the interfacial energy σ if the precipitate shape remained spherical.

3. Strength model

When building a strength model for Al-Cu alloys, the particles are the precipitates with a shape corresponding approximately to cuboid plates aligned with $\{001\}$ aluminum matrix planes, see e.g. in Ref. [40]. Let the half-diagonal of the particles be denoted r. Such particles, aligned with on $\{001\}$ planes, will interact with dislocations gliding on the $\{111\}$ planes, provided the center of the particle is closer than $\sqrt{3}r/3$ from the $\{111\}$ slip plane, as illustrated in Figure 4. The cross-sectional area that is intersected by the glide plane, varies with how close the particle is located. A statistical distribution of the particle half-diagonal is considered. A density $\phi(r)$ denotes the number of particles of size r per volume and per half-diagonal length. Hence $\int_0^\infty \phi dr = N_V$, where N_V is the number of particles per volume.

A small area δA of the (111) slip plane is considered in Figure 4. Particles with size r aligned not only with (001), but also (100) or (010), will pierce this glide plane if they are located closer than $\pm\sqrt{3}r/3$ away from it. Note that this is an estimate for thin particles; this length will change with increased thickness, towards $\pm r$ for spherical particles. A control volume $\delta V = \delta A\, 2\sqrt{3}r/3$ contains all such particles, as sketched in Figure 4. The expected number of such intersecting particles in this control volume, i.e. particles of size between $r - dr/2$ and $r + dr/2$ that intersects the slip plane area δA, can be expressed from the statistical distribution.

$$dN_r = \delta A \frac{2\sqrt{3}}{3} r\phi\, dr \tag{20a}$$

The density of particle-based pinning points per area slip plane is denoted n. The density of pinning points per area slip plane of size between $r - dr/2$ and $r + dr/2$ is denoted dn. Then the number of particles of size between $r - dr/2$ and $r + dr/2$ that intersects the slip plane area δA, can alternatively be expressed

$$\delta A\, dn = \zeta dN_r = \delta A \frac{2\zeta\sqrt{3}}{3} r\phi\, dr \tag{20b}$$

When the distance between the particles is significantly larger than r, each particle intersection of the slip plane counts as one pinning point, corresponding to $\zeta = 1$. However, when the particles are close to each other, which is the case close to peak hardness, the width of the particle matters. When the distance between the plates is of the same order of magnitude as r, a simple estimate would be to model the plate as four needles along its edges. This corresponds to $\zeta = 4$. It follows that the density of pinning points per area slip plane, n, i.e. the number of intersecting particles per area slip plane, equals

$$n = \int_0^n dn = \int_0^\infty \frac{2\zeta\sqrt{3}}{3} r\phi dr = \frac{2\zeta\sqrt{3}}{3} \overline{r} N_V \tag{21}$$

Here, $\overline{r}$ is the average particle radius. The particles act as obstacles for the dislocation movement. Their non-dimensional obstacle strength is $f = \cos(\phi_c/2)$, where ϕ_c is the critical breaking angle of the dislocation. The largest particles are non-shearable with $f = 1$, whereas the dislocations can glide through sufficiently weak, shearable particles. The energy required for cutting increases with increasing area of the section of the particle that the dislocation cuts through. Furthermore, the dislocation cuts the particle obliquely. Depending on the line direction of the dislocation as compared to the particle orientation, a certain length of the dislocation has to cut (glide) through the particle. This will be a length between the thickness and the width of the intersected plane of the plate type of particle. When doing so, a one Burgers vector step of new particle interface area is created on entering and leaving, and the internal structure of the particle is modified. The details are complicated and not fully explored. We will here make the pragmatic and simple assumption that the non-dimensional obstacle strength increases proportionally to the cross-sectional area of the particle that the dislocation has to cut. However, at a certain critical area, a_c, the particle will act as a strong particle.

The average strength of all particles or pinning points experienced by a slip plane area δA, can be expressed

$$\overline{f} = \frac{\int_0^\infty \delta A f_r dn}{\int_0^\infty \delta A dn} = \frac{\int_0^\infty f_r \frac{2\zeta\sqrt{3}}{3} \phi r dr}{\int_0^\infty \frac{2\zeta\sqrt{3}}{3} \phi r dr} = \frac{1}{\overline{r} N_V} \int_0^\infty f_r \phi r dr \tag{22}$$

Here f_r is the average cutting strength of a particle of half-diagonal r. Note that the average strength values for all particles and for pinning points are the same.

A correlation between particle thickness t and half-diagonal r is assumed

$$\Omega = \frac{r}{t} \tag{23}$$

It is assumed that the cutting strength depends on the cut area as

$$f = \min\left(\frac{a}{a_c}, 1\right) \tag{24}$$

The cross-sectional area a of a cuboid plate varies with where the dislocation cuts it, with a maximum when it glides through the particle center. One particle contributes with many pinning potential points, one for each slip-plane intersection. Each intersection corresponds to a specific cutting strength. Hence, the same particle can act as both a strong or weak pinning point for different slip planes cutting through. The average cutting strength of a particle of radius r is

$$f_r = \frac{1}{r}\int_0^r f dz = \frac{1}{r}\int_0^r \min\left(\frac{a}{a_c}, 1\right) dz \tag{25}$$

For the cuboid plate with max thickness t and diagonal $2r$, the cut area through the particle varies linearly with the distance z between the particle center and where the glide plane intersects the major axis, i.e. $a = \sqrt{6}t(r - |z|)/2$. The max area is $a_{max} = \sqrt{6}rt/2$. When $a_{max} > a_c$, the critical area size will occur at $z_c = r - \sqrt{6}a_c/(3t)$. The average pinning point strength for all glide planes being cut, is

$$f_r = \begin{cases} \dfrac{\sqrt{6}rt}{4a_c}, & \dfrac{\sqrt{6}rt}{2} < a_c \\ 1 - \dfrac{\sqrt{6}a_c}{6rt}, & \dfrac{\sqrt{6}rt}{2} \geq a_c \end{cases} \tag{26}$$

Finally, based on discrete dislocation simulations, the strength contribution σ_p from the particles can be expressed [39]

$$\sigma_p = 0.9M\mu b\sqrt{n}\,\bar{f}^{\frac{3}{2}}\left(1 - \frac{1}{6}\bar{f}^{5}\right) \tag{27}$$

where M is the Taylor factor. μ is the aluminum shear modulus, and b is the Burgers vector. $M = 3,\ \mu = 22.8\,GPa,\ b = 0.286\,nm$ will be used. Thus, the overall yield strength σ_y is calculated by summing three contributions:

$$\sigma_y = \sigma_0 + \sigma_{ss} + \sigma_p \tag{28}$$

where σ_0 is the intrinsic strength of Al, equal to 45 MPa [41]; σ_{ss} is the contribution from solid solution strengthening, described by

$$\sigma_{ss} = \sum_i K_i c_i^{m\,2/3} \tag{29}$$

where K_i is a constant related to the size, modulus and electronic mismatch of a specific solute element. The value of 60 $\mathrm{MPa/(wt.\%)^{2/3}}$ will be used for the Cu element, which is derived from the measured initial yield strength [41, 42]. A slightly smaller value of 46.4 $\mathrm{MPa/(wt.\%)^{2/3}}$ has been used in [3, 4] for the solid solution effect from Cu elements.

When building a strength model for η' phases in Al-Zn-Mg alloys, the particles are the precipitates with a shape corresponding approximately to cuboid plates aligned with $\{111\}$ aluminum matrix planes [18]. Correspondingly, the Eqs. 21 and 26 are modified, respectively:

$$n = \int_0^n dn = \int_0^\infty \frac{1}{\Omega} r\phi dr = \frac{1}{\Omega}\bar{r}N_V \tag{30}$$

$$f_r = \begin{cases} \dfrac{2r^2}{a_c}, & 2r^2 < a_c \\ 1, & 2r^2 \geq a_c \end{cases} \tag{31}$$

The values of K for Mg and Zn elements are chosen as 20 and 3 $\mathrm{MPa/(wt.\%)^{2/3}}$, respectively [43].

4. Models application

4.1. Experimental data

The Al-4.62 wt.% Cu-0.65 wt.% Mg (Al-2.01 at.% Cu-0.74 at.%) alloys studied earlier in Ref. [26] were selected to verify the extended KWN model. As reported in Ref. [26], the dominant precipitates are disk-shaped θ' phases in the alloy, while the Mg containing S′-Al2CuMg phase is insignificant. Hence the alloy is here in the modelling approximated as a binary Al-4.62 wt.% Cu (Al-2.015 at.% Cu) alloy. The reported experimental microstructure results for the aging at 513.15K for about 4h [26] are listed in Table 1.

The extended KWN model is also applicable to multi-component aluminum alloys. An example of the Al-6.1 wt.% Zn-2.35 wt.% Mg alloys aged at 433.15K with a fast heating rate was used [44, 45]. Note that the considered material was undeformed, and the evolution of precipitate mean radius and microhardness with time was reported. The dominant precipitates are plate-shaped η' phases in the alloy.

4.2. Study of the extended KWN model behavior

The extended KWN model was applied to simulate the precipitation kinetics of the disk-shaped θ' phases from the binary Al–4.62 wt.% Cu alloy during aging heat treatment. The classical heterogeneous nucleation law was adopted. The nucleation law has been described in detail in Ref. [16]. One of the important input parameters to the nucleation model is the number of heterogeneous nucleation sites. The parameter was assumed to correspond to the measured maximum particle number density, 570 μm^{-3}, which is the number density close to 0.25 hours aging treatment. In addition to the number of heterogeneous nucleation sites, the other key input parameter to the KWN model is the interfacial energy, σ, which affects both incubation time and coarsening rates. Based on a literature survey [46], the interfacial energy for the θ' phase ranges from 0.03 to 0.67 J/m^2. The value of 0.06 J/m^2 was chosen in the simulation. All input parameters used in the model are listed in Table 2.

Two different assumptions about the precipitates shape were used: the spherical shape and the oblate shape with a constant aspect ratio of 0.05. Note that the measured aspect ratios vary from 0.03 to 0.1 [16], so the middle value of 0.05 was chosen as the one used in our simulation. As can be seen from Figure 3, there is a slight difference (about 1.3) using different treatments for the curvature effect at this aspect ratio. In this study, the novel mean curvature method is used to treat the curvature effect, i.e. using Eq.18a. The predicted volume fraction and mean volume-equivalent spherical radius of the θ' phase are compared with

experimental measurements in Figures 5 and 6, respectively. The KWN model with the oblate shape assumption predicts higher volume fraction and larger mean radius of the θ' phase than with the spherical-shape assumption at the same aging time and agrees much better with the measured volume fraction and mean radius of precipitates.

Predicted distributions of the precipitate size are shown in Figure 7. The distributions for spheroid and oblate precipitates can both be well fitted by log-normal distributions. It should be pointed out that no measured data on the size distribution of precipitates was reported in Ref. [26]. To further test the strength model, a measured size distribution of oblate precipitates of an Al-3 wt.% Cu-0.05 wt.% Sn alloys aged at 473K for 1 hour [35], as shown in Figure 7 (c), will also be input into the strength model. Note that the main hardening particles in this alloy are also θ' phases.

The proposed KWN model is also applied to predict the growth process of the plate-shaped η' phases in ternary Al-6.1 wt.% Zn-2.35 wt.% Mg alloys aged at 433.15K. Due to limited experimental data, the input parameters are obtained mainly by tuning with available experimental results. The number of heterogeneous nucleation sites and the interfacial energy of the η' phase are chosen as 4.0×10^{5} μm^{-3} and 0.08 J/m^2, respectively. The constant aspect ratio of 0.6 is used in this simulation. The predicted mean volume-equivalent spherical radius of the η' phase is compared with the experimental results from small angle scattering, as shown in Figure 8. Similarly, the KWN model with the oblate shape assumption well predicts the mean radius of the η' phase.

4.3 Application of the strength model

It is commonly assumed that the critical size for the transition from shearable to non-shearable precipitates is close to the average size of the precipitates in the peak aged stage [9, 39, 47]. This is also assumed here, as input for the strength model, i.e. the value corresponding to the critical transition line plotted in Figure 7 is used as an input to the strength model below.

The strength model was applied to predict the evolution of yield strength during the aging process of the considered Al–4.62 wt.% Cu alloys at 513.15K. By comparison, the distributions using the spherical assumption were used as input and applying the strength model for spherical particles reported in [39]. Predicted results for both these strength models are compared with the experiments and shown in Figure 9. Note that the overaged stage is not included, because coarsening is not considered in this study.

As can be seen from Figure 9 (a), the proposed model with the oblate shape assumption predicts a smaller contribution from solid solution strengthening and a larger contribution from precipitation than the spherical assumption. In total, the yield strength is underestimated

using the spherical assumption, while the results using the oblate assumption match well with the measured values, as seen in Figure 9 (b). Note that the contribution from solid solution strengthening is relatively large in Al–4.62 wt.% Cu alloys as compared to AA6082 [39], which is attributed to much higher solute content in the matrix of Al–4.62 wt.% Cu alloys during the aging treatment. In fact, the Liu et al.'s model in Ref. [26] also exhibited a good prediction of the alloy's yield strength evolution, but it was based on a constant, overestimated value of the solid solution strengthening. Thus, it is reasonable to assume that their estimate of the strength contribution from hardening particles was too small.

To further verify the applicability of the proposed strength model, it was also applied to predict the yield strength of an Al-3Cu-0.05Sn alloy aged at 473K for 1 hour, using the measured size distribution of precipitates (Figure 7 (c)) reported in [35]. The critical transition size was chosen as the average size of the precipitates in the peak aged stage (4 hours). The predicted yield strength, 200MPa, matches very well the measured value. It should be pointed out, that the contribution from solid solution strengthening as predicted in Ref. [35], was significantly underestimated to be only about 4 MPa at 1 hour, hence their estimate of the strength contribution from precipitates must have been overestimated. Recently, Colombo et al. [36] reused the same strength model and parameters as in Ref. [35] and the same overestimation of the particle contribution should be expected.

The strength model was also applied to predict the evolution of yield strength during the aging process of ternary Al-6.1 wt.% Zn-2.35 wt.% Mg alloys at 433.15K. When the average size of the precipitates in the peak aged stage ($r = 4.1$ nm) is chosen as the critical transition size, the contribution from precipitation is overestimated. Thus, a slightly higher value ($r = 4.9$ nm) is chosen. The predicted yield strength is compared with the experiments and shown in Figure 10. The results using the oblate assumption match well with the measured values, suggesting that the proposed modeling framework is also applicable to multi-component system.

5. Discussion

An integrated microstructural and strength modeling framework for oblate-shaped precipitates has been proposed in this study. The entire framework is summarized in the flowchart as shown in Figure 11. The extended KWN model is able to predict the size distribution of oblate-shaped precipitates, which is used as input for the subsequent strength prediction. The classical CALPHAD-coupled KWN model is extended to account for the geometrical shape of the precipitates by the use of two correction factors (Figures 2 and 3), and thus it can provide reliable microstructural information (Figures 5, 6, 7, and 8) for the strength prediction. Note that the CALPHAD databases could be built on the base of first

principle calculations and thus their coupling with the KWN model is a scale-bridging feature [16]. The importance of the precipitates shape on the precipitation kinetics is emphasized by comparing the predicted results using two different assumptions, as shown in Figures 5, 6 and 7. The spherical assumption will underestimate the growth process of the oblate-shaped precipitates.

As mentioned in Section 2, the two correction factors in the extended KWN model have opposite effects on the growth rate of disk-shaped particles. The first one, based on the solution of the diffusion problem, increases the growth, because of the enhancement of the solute atom transportation rate to the growth interface. The second one, related to the Gibbs Thomson correction, decreases the growth compared to spherical particles, by suppression of the super-saturation for growth. As can be seen from Figures 5 and 6, the positive effect on the growth of the first correction factor overwhelms the negative effect of the second correction factor. In total, this leads to more rapid growth using the oblate shape assumption.

Recently, another correction factor for the Gibbs-Thomson effect was given in [30, 31]. If applied to the coherent precipitates as the case here, their correction factor ignores the effect from crystallographic growth constraints as explained in the introduction. However, having taken the coherent elastic strain energy and interfacial energy anisotropy into account, the treatment in [30, 31] is interesting and worthy of further exploring.

Some unconformities between experimental data and predicted results can be observed in Figures 5 and 6, especially after 2 hours. One uncertainty is attributed to the measurement error, which was not assessed in Ref. [26]. This error is often considerable, estimated to be up to 40% in [16]. It should be pointed out that it is challenging to accurately measure the size of non-spherical particles. Another error source is the thermodynamic database accuracy. The measured volume fraction of precipitates after 4 hours aging should be very close to the equilibrium fraction. However, the equilibrium fraction given by the database is 0.047, which is 30% greater than the experimental value. Moreover, the extended KWN model does not consider the elastic strain energy and interfacial energy anisotropy effects, which also affect the accuracy of prediction.

Knowing the alloy composition, the amount of Cu in solid solution can be calculated by the proposed KWN model, and the contribution to the solid solution strengthening is given by Eq. 29. Also, the strength contribution from precipitates, obtained by Eq. 27, is based on the size distributions of precipitates. The proposed strength model for the oblate-shaped particles accurately predicts the contributions from hardening particles and solid solution strengthening which were underestimated or overestimated in previous works [26, 35, 36]. The significance of releasing the spherical assumption is further emphasized by comparing

the strength predictions from two kinds of assumptions (Figure 9). The advantage of the proposed strength model comes from considering that a disk-shaped particle with the same volume as a spherical one pierces more slip planes, i.e. from Eq. 21. Last but not least, the size distributions of precipitates bridge the microstructural and strength prediction models. This bridging factor makes the predictions become more real and accurate.

The importance of including the precipitate's morphology in the modeling has been emphasized in this study. The proposed model is rather simple with a minimum of tuning parameters, making it efficient and applicable. The surface energy anisotropy of the particles is not considered, as it would have to be matched by a more complex diffusion solution to predict anisotropic particle growth. The proposed modeling framework has also been successfully applied to the ternary Al-Mg-Zn system, and some reasonable predictions are made (Figures 8 and 10). However, these are based on some assumed input parameters, like the number of heterogeneous nucleation sites and critical transition size. In the future, the framework will be adapted to more examples and more complex models, e.g. for the multi-phase case [16], and other metals.

6. Conclusions

A new integrated microstructural and strength prediction framework has been developed for disk-shaped precipitates. It has been applied to simulate the aging process of Al-Cu and Al-Mg-Zn alloys. The main conclusions are listed below:

- Two correction factors for the oblate-spheroid or cuboid plate-shaped particles are calculated for the extended KWN microstructural model. They have opposite influences on the growth kinetics of oblate-shaped as compared to spheroid-shaped particles. The correction factor for growth rate has a positive effect on the growth kinetics, while the correction factor for the Gibbs-Thomson effect has a negative effect.
- Oblate-shaped precipitates grow faster than spherical precipitates with equivalent volume and contribute more to the precipitation strengthening. Improved agreement with the reported experimental results is obtained.
- The proposed strength model takes into account the size distributions and shape of harding particles. It has achieved a better prediction accuracy than the previous models reported in Refs. [26, 35, 36]. It can predict the strength contribution from precipitates without a tuning parameter for the mean particle spacing in the slip plane. The particle size distribution plays an important role in bridging the microstructural and strength models.

Declaration of interest
None

Qiang Du on behalf of all the authors

Acknowledgments

This work was supported by the AMPERE project (247783), a Knowledge-building Project for Industry, co-financed by The Research Council of Norway, and the industrial partners Norsk Hydro, Sapa, Gränges, Neuman Aluminium Raufoss (Raufoss Technology) and NEXANS. Yue Li was supported by the China Scholarship Council and Research Council of Norway as a joint training Ph. D student in SINTEF/NTNU, Norway.

References

[1] H.S. Hasting, A.G. Frøseth, S.J. Andersen, R. Vissers, J.C. Walmsley, C.D. Marioara, F. Danoix, W. Lefebvre, R. Holmestad, Composition of β″ precipitates in Al-Mg-Si alloys by atom probe tomography and first principles calculations, J. Appl. Phys. 106(12) (2009) 123527.
[2] A. Biswas, D.J. Siegel, C. Wolverton, D.N. Seidman, Precipitates in Al–Cu alloys revisited: Atom-probe tomographic experiments and first-principles calculations of compositional evolution and interfacial segregation, Acta Mater. 59(15) (2011) 6187-6204.
[3] O.R. Myhr, Ø. Grong, S.J. Andersen, Modelling of the age hardening behaviour of Al–Mg–Si alloys, Acta Mater. 49(1) (2001) 65-75.
[4] O. Myhr, Ø. Grong, H. Fjaer, C. Marioara, Modelling of the microstructure and strength evolution in Al–Mg–Si alloys during multistage thermal processing, Acta Mater. 52(17) (2004) 4997-5008.
[5] S. Esmaeili, D.J. Lloyd, W.J. Poole, Modeling of precipitation hardening for the naturally aged Al-Mg-Si-Cu alloy AA6111, Acta Mater. 51(12) (2003) 3467-3481.
[6] Q. Du, B. Holmedal, J. Friis, C.D. Marioara, Precipitation of non-spherical particles in aluminum alloys Part II: numerical simulation and experimental characterization during aging treatment of an Al-Mg-Si alloy, Metall. Mater. Trans. A 47(1) (2016) 589-599.
[7] A. Bahrami, A. Miroux, J. Sietsma, An age-hardening model for Al-Mg-Si alloys considering needle-shaped precipitates, Metall. Mater. Trans. A 43(11) (2012) 4445-4453.
[8] B. Holmedal, E. Osmundsen, Q. Du, Precipitation of Non-Spherical Particles in Aluminum Alloys Part I: Generalization of the Kampmann–Wagner Numerical Model, Metall. Mater. Trans. A 47(1) (2016) 581-588.
[9] D. Bardel, M. Perez, D. Nelias, A. Deschamps, C.R. Hutchinson, D. Maisonnette, T. Chaise, J. Garnier, F. Bourlier, Coupled precipitation and yield strength modelling for non-isothermal treatments of a 6061 aluminium alloy, Acta Mater. 62 (2014) 129-140.
[10] K. Kim, A. Roy, M.P. Gururajan, C. Wolverton, P.W. Voorhees, First-principles/Phase-field modeling of θ′ precipitation in Al-Cu alloys, Acta Mater. 140 (2017) 344-354.
[11] K. Tang, Q. Du, Y. Li, Modelling microstructure evolution during casting, homogenization and ageing heat treatment of Al-Mg-Si-Cu-Fe-Mn alloys, Calphad 63 (2018) 164-184.
[12] Q. Du, Y. Li, An extension of the Kampmann–Wagner numerical model towards as-cast grain size prediction of multicomponent aluminum alloys, Acta Mater. 71(0) (2014) 380-389.
[13] Q. Du, W. Poole, M. Wells, N. Parson, Microstructure evolution during homogenization of Al–Mn–Fe–Si alloys: Modeling and experimental results, Acta Mater. 61(13) (2013) 4961-4973.

[14] C.L. Liu, H. Azizi-Alizamini, N.C. Parson, W.J. Poole, Q. Du, Microstructure evolution during homogenization of Al-Mg-Si-Mn-Fe alloys: Modelling and experimental results, Trans. Nonferrous Met. Soc. China 27(4) (2017) 747-753.
[15] C.L. Liu, Q. Du, N.C. Parson, W.J. Poole, The interaction between Mn and Fe on the precipitation of Mn/Fe dispersoids in Al-Mg-Si-Mn-Fe alloys, Scripta Mater. 152 (2018) 59-63.
[16] Q. Du, K. Tang, C.D. Marioara, S.J. Andersen, B. Holmedal, R. Holmestad, Modeling over-ageing in Al-Mg-Si alloys by a multi-phase CALPHAD-coupled Kampmann-Wagner Numerical model, Acta Mater. 122 (2017) 178-186.
[17] S. Wang, M. Starink, Two types of S phase precipitates in Al–Cu–Mg alloys, Acta Mater. 55(3) (2007) 933-941.
[18] G. Sha, A. Cerezo, Early-stage precipitation in Al–Zn–Mg–Cu alloy (7050), Acta Mater. 52(15) (2004) 4503-4516.
[19] J.-F. Nie, Precipitation and Hardening in Magnesium Alloys, Metall. Mater. Trans. A 43(11) (2012) 3891-3939.
[20] Y.M. Zhu, A.J. Morton, J.F. Nie, The 18R and 14H long-period stacking ordered structures in Mg–Y–Zn alloys, Acta Mater. 58(8) (2010) 2936-2947.
[21] K. Kulawik, P.A. Buffat, A. Kruk, A.M. Wusatowska-Sarnek, A. Czyrska-Filemonowicz, Imaging and characterization of γ' and γ'' nanoparticles in Inconel 718 by EDX elemental mapping and FIB-SEM tomography, Mater. Charact. 100 (2015) 74-80.
[22] T. Hu, J.H. Chen, J.Z. Liu, Z.R. Liu, C.L. Wu, The crystallographic and morphological evolution of the strengthening precipitates in Cu–Ni–Si alloys, Acta Mater. 61(4) (2013) 1210-1219.
[23] F.S. Ham, Theory of diffusion-limited precipitation, J. Phys. Chem. Solids 6(4) (1958) 335-351.
[24] G. Horvay, J.W. Cahn, Dendritic and spheroidal growth, Acta Metall. 9(7) (1961) 695-705.
[25] Y.H. Chen, R.D. Doherty, On the growth kinetics of plate-shaped precipitates in aluminium-copper and aluminium-gold alloys, Scr. Metall. 11(9) (1977) 725-729.
[26] G. Liu, G. Zhang, X. Ding, J. Sun, K. Chen, Modeling the strengthening response to aging process of heat-treatable aluminum alloys containing plate/disc-or rod/needle-shaped precipitates, Mater. Sci. Eng., A 344(1) (2003) 113-124.
[27] Y. Hu, G. Wang, M. Ye, S. Wang, L. Wang, Y. Rong, A precipitation hardening model for Al-Cu-Cd alloys, Mater. Des. 151 (2018) 123-132.
[28] D. Wolf-Gladrow, U. Riebesell, Diffusion and reactions in the vicinity of plankton: a refined model for inorganic carbon transport, Mar. Chem. 59(1-2) (1997) 17-34.
[29] F.S. Ham, Diffusion‐Limited Growth of Precipitate Particles, J. Appl. Phys. 30(10) (1959) 1518-1525.
[30] Precipitation Module (TC-PRISMA) User Guide, Thermo-Calc Version 2018a, P95-96, http://www.thermocalc.com/support/documentation/.
[31] K. Wu, Q. Chen, P. Mason, Simulation of precipitation kinetics with non-spherical particles, J. Phase Equilib. Diffus. 39(5) (2018) 571-583.
[32] C.A. Johnson, Generalization of the Gibbs-Thomson equation, Surf. Sci. 3(5) (1965) 429-444.
[33] J.F. Nie, B.C. Muddle, I.J. Polmear, The effect of precipitate shape and orientation on dispersion strengthening in high strength aluminium alloys, Mater. Sci. Forum, 1996, pp. 1257-1262.
[34] S. Esmaeili, D. Lloyd, W. Poole, A yield strength model for the Al-Mg-Si-Cu alloy AA6111, Acta Mater. 51(8) (2003) 2243-2257.

[35] J. da Costa Teixeira, D.G. Cram, L. Bourgeois, T.J. Bastow, A.J. Hill, C.R. Hutchinson, On the strengthening response of aluminum alloys containing shear-resistant plate-shaped precipitates, Acta Mater. 56(20) (2008) 6109-6122.
[36] M. Colombo, E. Gariboldi, P. Bassani, M. Albu, F. Hofer, Modeling the Microstructural and Yield Strength Evolution of an Age-Hardenable Al Alloy for High Temperature Applications, Mater. Sci. Forum, 2017, pp. 380-385.
[37] J. Friedel, Dislocations, First ed., Pergamon Press, Oxford, 1964.
[38] U.F. Kocks, A.S. Argon, M.F. Ashby, Thermodynamics and kinetics of slip, Prog. Mater Sci. 19 (1975) 1-291.
[39] B. Holmedal, Strength contributions from precipitates, Philos. Mag. Lett. 95(12) (2015) 594-601.
[40] C. Liu, S.K. Malladi, Q. Xu, J. Chen, F.D. Tichelaar, X. Zhuge, H.W. Zandbergen, In-situ STEM imaging of growth and phase change of individual $CuAl_X$ precipitates in Al alloy, Sci. Rep. 7(1) (2017) 2184.
[41] H.R. Shercliff, M.F. Ashby, A process model for age hardening of aluminium alloys—I. The model, Acta Metall. Mater. 38(10) (1990) 1789-1802.
[42] H. Hardy, The ageing characteristics of binary Aluminium-Copper Alloys, J. Inst. Metals 79(11) (1951) 321-369.
[43] M. Dixit, R. Mishra, K. Sankaran, Structure–property correlations in Al 7050 and Al 7055 high-strength aluminum alloys, Mater. Sci. Eng., A 478(1-2) (2008) 163-172.
[44] A. Deschamps, Y. Brechet, Influence of predeformation and ageing of an Al–Zn–Mg alloy—II. Modeling of precipitation kinetics and yield stress, Acta Mater. 47(1) (1998) 293-305.
[45] A. Deschamps, F. Livet, Y. Bréchet, Influence of predeformation on ageing in an Al–Zn–Mg alloy—I. Microstructure evolution and mechanical properties, Acta Mater. 47(1) (1998) 281-292.
[46] S. Hu, M. Baskes, M. Stan, L. Chen, Atomistic calculations of interfacial energies, nucleus shape and size of θ' precipitates in Al-Cu alloys, Acta Mater. 54(18) (2006) 4699-4707.
[47] F. Fazeli, W.J. Poole, C.W. Sinclair, Modeling the effect of Al3Sc precipitates on the yield stress and work hardening of an Al–Mg–Sc alloy, Acta Mater. 56(9) (2008) 1909-1918.
[48] Q. Du, M. Perez, W.J. Poole, M. Wells, Numerical integration of the Gibbs–Thomson equation for multicomponent systems, Scripta Mater. 66(7) (2012) 419-422.

Appendix A

In Chen and Doherty's study [25], the functions of the radius, r_0, and the half of thickness, $L/2$, with time t for the oblate spheroid are given:

$$r_0 = 2\sqrt{\frac{1}{\alpha^2}\beta D t} \tag{A1}$$

$$\frac{L}{2} = 2\sqrt{\beta D t} \tag{A2}$$

$$\Omega = \exp(\beta)\beta^{3/2}\frac{1}{\alpha^2}\int_{\beta}^{\infty}\frac{\exp(-\mu)\mathrm{d}\mu}{\left(\beta\left(\frac{1}{\alpha^2}-1\right)+\mu\right)\mu^{1/2}} = \frac{\Delta c_i}{\left(c_i^m + \Delta c_i - c_i^p\right)} \tag{A3}$$

where Ω is the supersaturation. β is a dimensionless growth parameter. Thus, the function of volume with time for the oblate spheroid is given:

$$V = \frac{4\pi}{3}{r_0}^2\frac{L}{2} = \frac{32\pi}{3\alpha^2}(\beta D t)^{\frac{3}{2}} \tag{A4}$$

The rates of the volume change of the oblate spheroid ($\dot{V}_{\text{Chen}}^{\text{oblate}}$) and the equivalent volume sphere ($\dot{V}_{\text{Chen}}^{\text{spherical}}$) are derived:

$$\dot{V}_{\text{Chen}}^{\text{oblate}} = \frac{16\pi}{\alpha^2}(\beta D)^{\frac{3}{2}}\sqrt{t} \tag{A5}$$

$$\dot{V}_{\text{Chen}}^{\text{spherical}} = \frac{4\pi D\Delta c_i}{\left(c_i^m + \Delta c_i - c_i^p\right)}\sqrt[3]{{r_0}^2\frac{L}{2}} = \frac{8\pi}{\sqrt[3]{\alpha^2}}\Omega(D)^{\frac{3}{2}}\sqrt{\beta t} \tag{A6}$$

Thus,

$$f(\alpha)_{\text{Chen}} = \frac{\dot{V}_{\text{Chen}}^{\text{oblate}}}{\dot{V}_{\text{Chen}}^{\text{spherical}}} = \frac{2}{\Omega}\alpha^{-\frac{4}{3}}\beta \tag{A7}$$

In Liu et al.'s study [26], the functions of the radius, r_0, and the half of thickness, $L/2$, with time t for the oblate spheroid are given:

$$r_0 = \frac{2}{3}\sqrt{\frac{1}{\alpha^2}\beta D t} \tag{A8}$$

$$\frac{L}{2} = \frac{2}{3}\sqrt{\beta D t} \tag{A9}$$

$$\beta = \frac{3\alpha}{2}\frac{\Delta c_i}{\left(c_i^m + \Delta c_i - c_i^p\right)} \tag{A10}$$

Thus, the function of volume with time for the oblate spheroid is given:

$$V = \frac{4\pi}{3}{r_0}^2\frac{L}{2} = \frac{32\pi}{81\alpha^2}(\beta D t)^{\frac{3}{2}} \tag{A11}$$

The rates of the volume change of the oblate spheroid ($\dot{V}^{oblate}{}_{Liu}$) and the equivalent volume sphere ($\dot{V}_{\text{Liu}}^{\text{spherical}}$) are derived:

$$\dot{V}_{\mathrm{Liu}}^{\mathrm{oblate}} = \frac{8\pi}{9\sqrt{\alpha}}\left(\frac{D_i \Delta c_i}{\left(c_i^m + \Delta c_i - c_i^p\right)}\right)^{\frac{3}{2}} \sqrt{\frac{3t}{2}} \tag{A12}$$

$$\dot{V}_{\mathrm{Liu}}^{\mathrm{spherical}} = \frac{4\pi D \Delta c_i}{\left(c_i^m + \Delta c_i - c_i^p\right)} \sqrt[3]{\frac{L{r_0}^2}{2}} = \frac{8\pi}{3\sqrt[6]{\alpha}} \left(\frac{D \Delta c_i}{c_i^m + \Delta c_i - c_i^p}\right)^{\frac{3}{2}} \sqrt{\frac{3t}{2}} \tag{A13}$$

Thus,

$$f(\alpha)_{\mathrm{Liu}} = \frac{\dot{V}_{\mathrm{Liu}}^{\mathrm{oblate}}}{\dot{V}_{\mathrm{Liu}}^{\mathrm{spherical}}} = \frac{1}{3\sqrt[3]{\alpha}} \tag{A14}$$

In Wolf-Gladrow and Riebesell's study [28], the flux of solute *i* through the precipitate interface for the oblate spheroid, J_i^{oblate}, and the flux for the equivalent volume sphere, $J_i^{\mathrm{spherical}}$, respectively:

$$J_i^{\mathrm{oblate}} = 4\pi D_i \Delta c_i r_{\mathrm{area}} = 2\pi D_i \Delta c_i \sqrt{2\left(r_0^2 + \frac{L^2}{4e}\ln\left(\frac{1+e}{\alpha}\right)\right)} \tag{A15}$$

And,

$$J_i^{\mathrm{spherical}} = 4\pi D_i \Delta c_i \sqrt[3]{\frac{L r_0^2}{2}} \tag{A16}$$

where r_{area} is the radius of a hypothetical sphere with the same surface area as the spheroid.

The rates of the volume change of the oblate spheroid ($\dot{V}_{\mathrm{W}}^{\mathrm{oblate}}$) and the equivalent volume sphere ($\dot{V}_{\mathrm{W}}^{\mathrm{spherical}}$) are derived, respectively:

$$\dot{V}_{\mathrm{W}}^{\mathrm{oblate}} = \frac{2\pi D_i \Delta c_i}{\left(c_i^m + \Delta c_i - c_i^p\right)} r_0 \sqrt{2\left(1 + \frac{\alpha^2}{e}\ln\left(\frac{1+e}{\alpha}\right)\right)} \tag{A17}$$

$$\dot{V}_{\mathrm{W}}^{\mathrm{spherical}} = \frac{4\pi D_i \Delta c_i}{\left(c_i^m + \Delta c_i - c_i^p\right)} \sqrt[3]{r_0^2 \frac{L}{2}} \tag{A18}$$

Thus,

$$f(\alpha)_{\mathrm{W}} = \frac{\dot{V}_W^{\mathrm{oblate}}}{\dot{V}_W^{\mathrm{spherical}}} = \frac{\sqrt{2\left(1 + \frac{\alpha^2}{e}\ln\left(\frac{1+e}{\alpha}\right)\right)}}{2\sqrt[3]{\alpha}} \tag{A19}$$

Figure captions

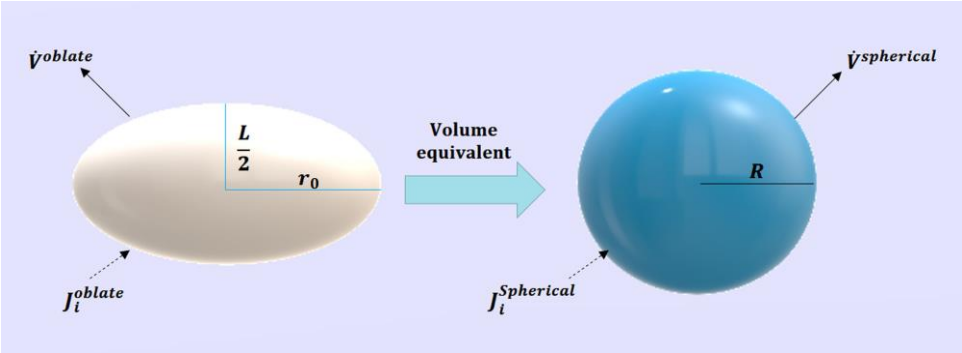

Figure 1 Schematic diagram of the oblate spheroid and its volume-equivalent sphere.

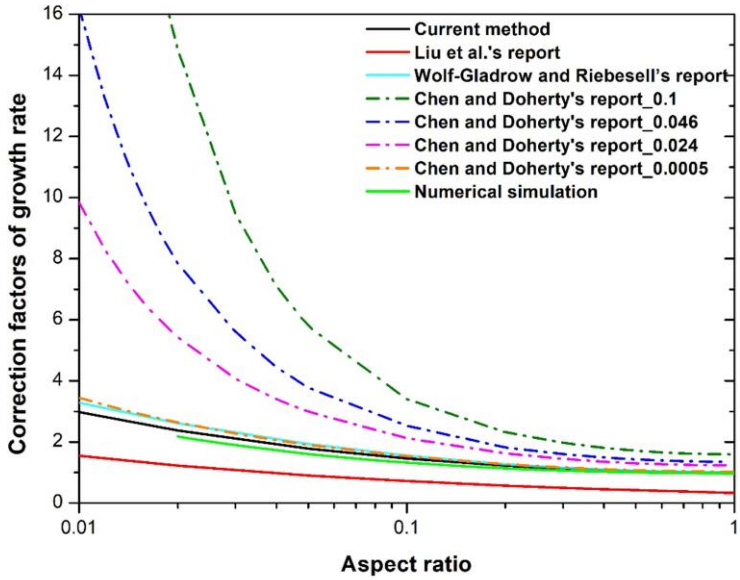

Figure 2 Dependences of correction factors of the growth rate on aspect ratios. For Chen and Doherty's report [25], the correction factors depending on supersaturation (from 0.0005 to 0.1) are shown.

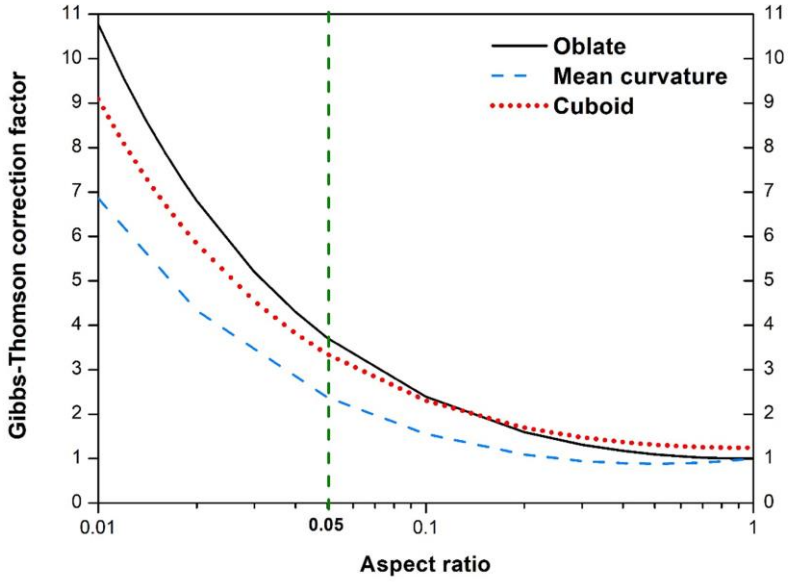

Figure 3 Dependences of the Gibbs-Thomson correction factors on the aspect ratios for three cases.

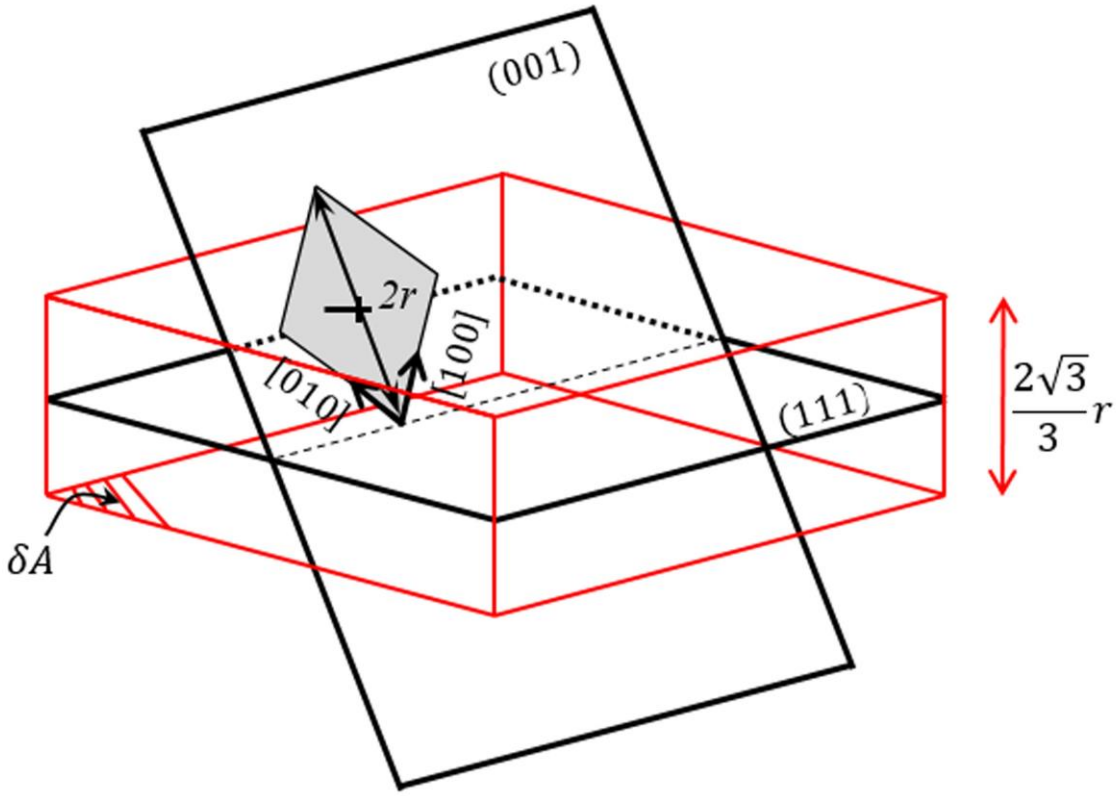

Figure 4 Schematic diagram of cuboid-plates particles aligned with {001} planes and interacting with dislocations gliding on the (111) plane.

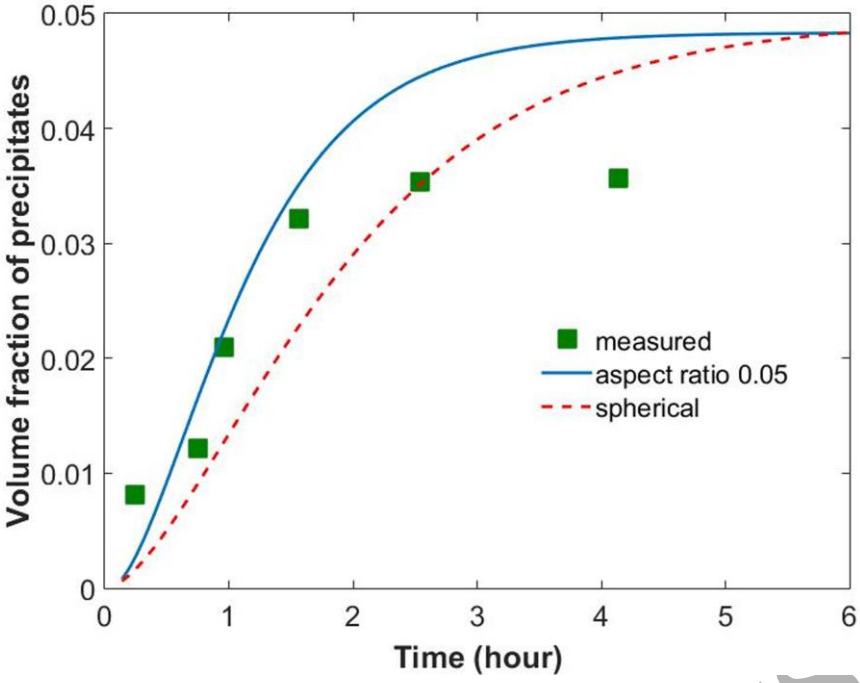

Figure 5 Experimental and predicted evolutions of the volume fraction of θ' phases during the aging process of Al–4.62 wt.% Cu alloys at 513.15K.

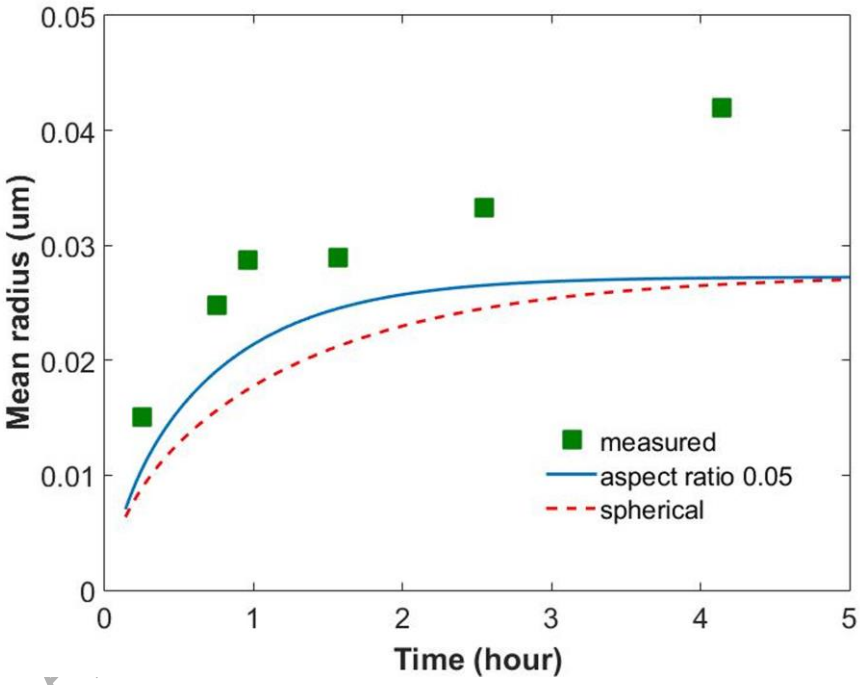

Figure 6 Experimental and predicted evolutions of the mean radius (equivalent volume) of θ' phases during the aging process of Al–4.62 wt.% Cu alloys at 513.15K.

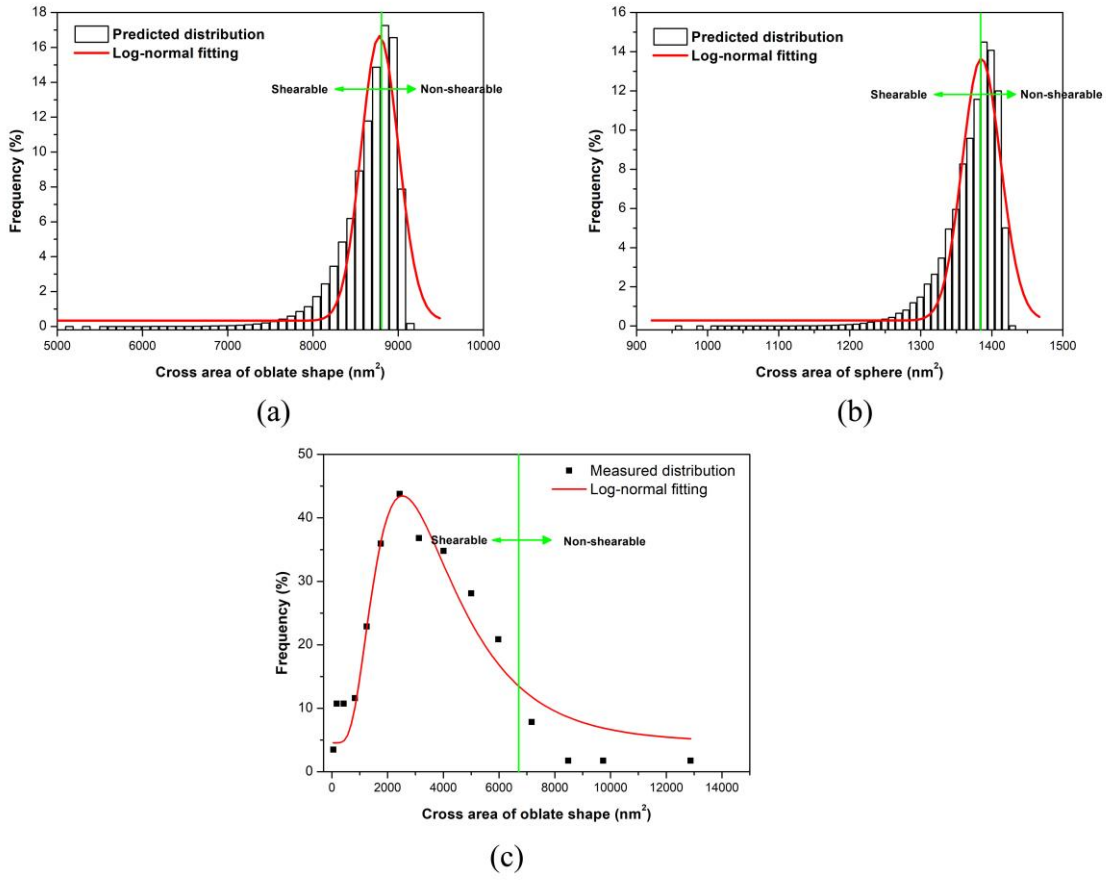

Figure 7 Predicted precipitates size distributions during the aging process of Al–4.62 wt.% Cu alloys at 513.15K for 1.5 hours (peak aging) using two kinds of assumptions: (a) the oblate shape with a constant aspect ratio of 0.05 and (b) the spherical shape; (c) measured size distribution of oblate precipitates of Al-3Cu-0.05Sn alloys aging at 473K for 1 hour [35]. These distributions are fitted by log-normal distributions. Note that the lines for the transition from shearable to non-shearable precipitates are also given.

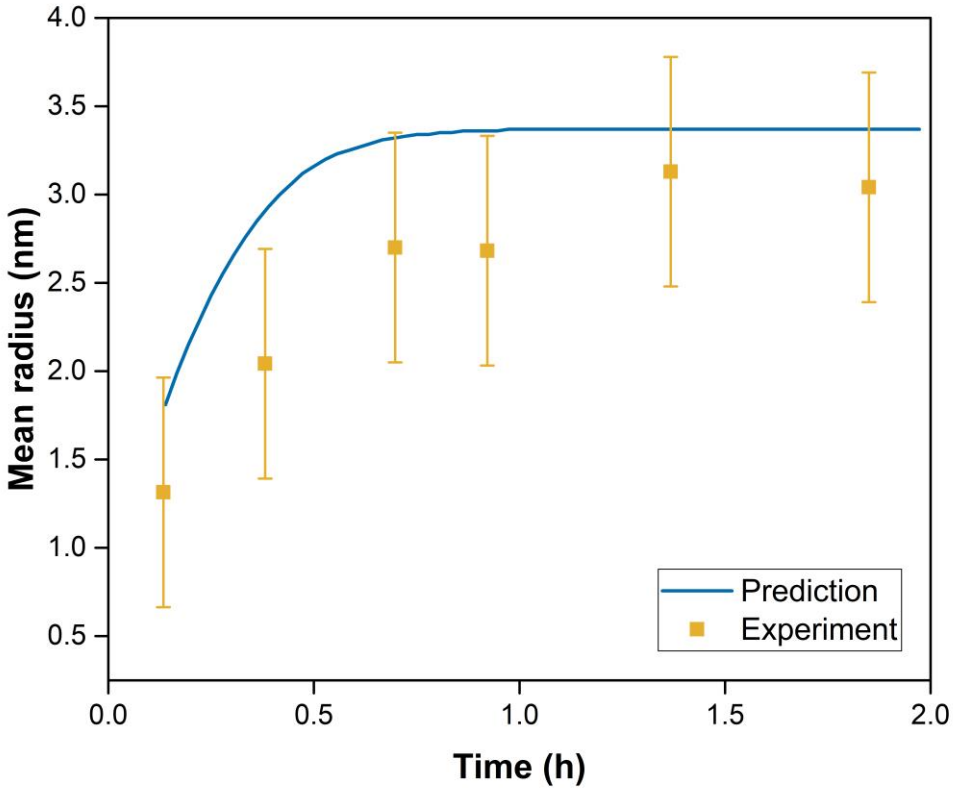

Figure 8 Predicted evolutions of the mean radius (equivalent volume) of η′ phases during the aging process of Al-6.1 wt.% Zn-2.35 wt.% Mg alloys at 433.15K.

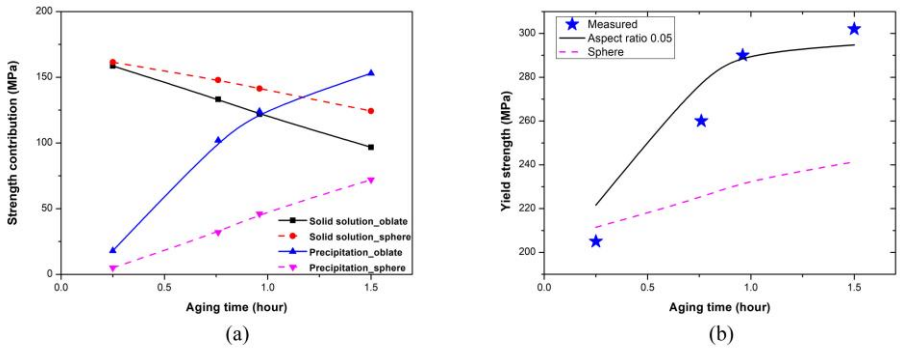

Figure 9 Predicted strength contributions from (a) solid solution and precipitation using two kinds of assumptions, and (b) comparison of measured [26] and predicted yield strength evolutions during the aging process of Al–4.62 wt.% Cu alloys at 513.15K.

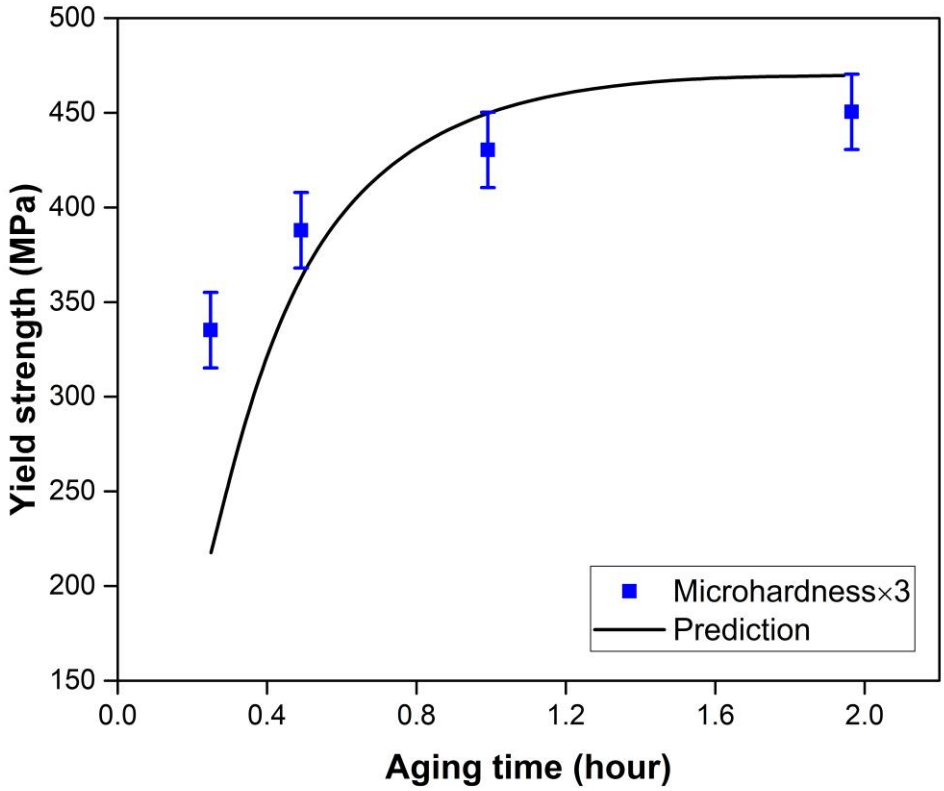

Figure 10 Comparison of measured [44, 45] and predicted yield strength evolutions during the aging process of Al-6.1 wt.% Zn-2.35 wt.% Mg alloys at 433.15K.

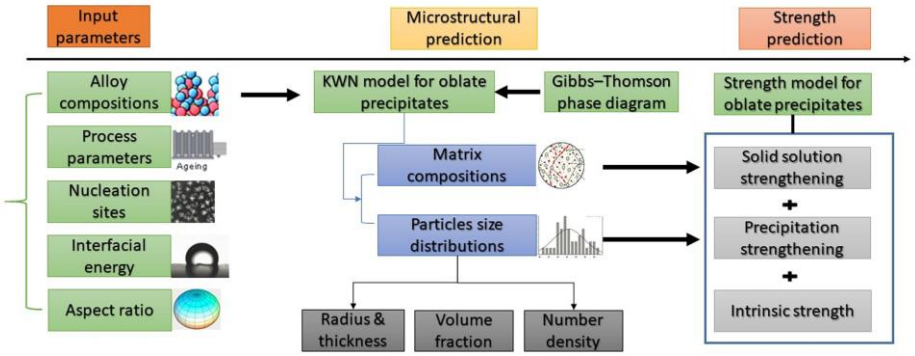

Figure 11 Flowchart of coupled microstructural and strength predictions for the oblate-shaped precipitates. Please refer to Ref. [48] for the concept "Gibbs–Thomson phase diagram". Note that the particle size distribution plays a crucial role in integrating different models.

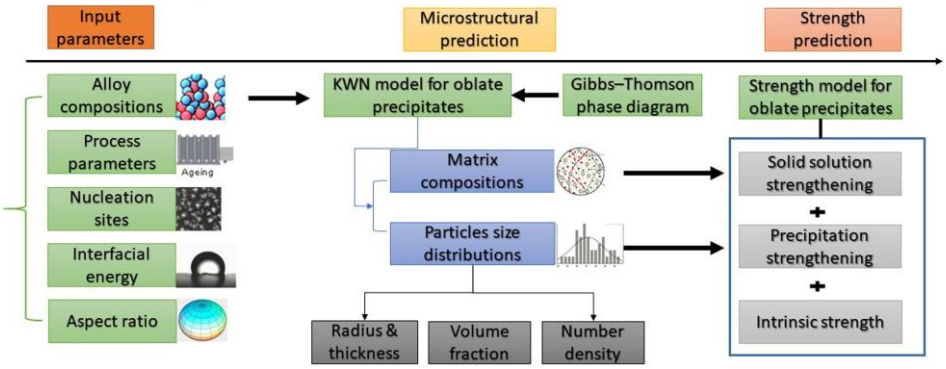

The flow chart for the coupled microstructure and strength prediction modeling framework in which the hardening particles disk shape and size distributions have been considered.

Graphical Abstract

Table captions

Table 1 Measured average precipitate radius, half of the thickness, aspect ratio, volume fraction, and yield strength [26].

Aging time (h)	Average radius (nm)	Average half of thickness (nm)	Aspect ratio	Volume fraction (%)	Yield strength (MPa)
0.25	32.5	3.2	0.1	0.81	205
0.76	59.7	4.3	0.07	1.22	260
0.96	78	3.9	0.05	2.09	290
1.57	90	3.0	0.03	3.22	302
2.55	100	3.7	0.037	3.53	290
4.14	119.48	5.2	0.04	3.56	270

Table 2 Input parameters used in the simulation.

Molar volume of θ', η', and FCC phases		0.9×10^{-5} m^3/mol	
Thermodynamic database		TCAL4 (Thermo-Calc)	
Diffusivities in the FCC phase		Diffusion constant (m^2/s)	Activation energy (kJ/mole)
	Cu	4.4×10^{-5}	133.9
	Mg	1.49×10^{-5}	120.5
	Zn	1.19×10^{-5}	116.1